Monthly Notices of the ROYAL ASTRONOMICAL SOCIETY

MNRAS **539,** 145–159 (2025) https://doi.org/10.1093/mnras/stae2773
Advance Access publication 2024 December 18

Spiral arm, rotating structure, and outflow cavity in massive star-forming region G23.43−0.18

James O. Chibueze [1,2★] Chukwuebuka J. Ugwu [1,2] Tomoya Hirota,[3,4] Kee-Tae Kim,[5,6] Tie Liu,[7] Jakobus M. Vorster,[8,9] Ji-hyun Kang,[5] Jungha Kim,[5,10] Ross A. Burns,[11] Andrey M. Sobolev [6,12] Jihye Hwang [5] Chang Won Lee,[5,13] Mi Kyoung Kim[14] and Koichiro Sugiyama[15,16]

[1]*Department of Mathematical Sciences, University of South Africa, Cnr Christian de Wet Rd and Pioneer Avenue, Florida Park, 1709 Roodepoort, South Africa*
[2]*Department of Physics and Astronomy, Faculty of Physical Sciences, University of Nigeria, Carver Building, 1 University Road, Nsukka 410001, Nigeria*
[3]*National Astronomical Observatory of Japan, National Institutes of Natural Sciences, 2-12 Hoshigaoka, Mizusawa, Oshu, Iwate 023-0861, Japan*
[4]*SOKENDAI (The Graduate University for Advanced Studies), 2-21-1 Osawa, Mitaka, Tokyo 181-8588, Japan*
[5]*Korea Astronomy and Space Science Institute, 776 Daedeokdaero, Yuseong, Daejeon 34055, Korea*
[6]*Xinjiang Astronomical Observatory, Chinese Academy of Sciences, Urumqi 830011, P. R. China*
[7]*Shanghai Astronomical Observatory, Chinese Academy of Sciences, 80 Nandan Road, Shanghai 200030, P. R. China*
[8]*Centre for Space Research, North-West University, Potchefstroom 2520, South Africa*
[9]*Department of Physics, University of Helsinki, PO Box 64, FI-00014 Helsinki, Finland*
[10]*Department of Astronomy and Space Science, Chungnam National University, Daejeon 34134, Korea*
[11]*RIKEN, Cluster for Pioneering Research, Wako-shi, Saitama, Japan*
[12]*Astronomical Observatory, Institute for Natural Sciences and Mathematics, Ural Federal University, 19 Mira Street, Ekaterinburg 620002, Russia*
[13]*University of Science and Technology, Korea (UST), 217 Gajeong-ro, Yuseong-gu, Daejeon 34113, Republic of Korea*
[14]*Department of Child Studies, Faculty of Home Economics, Otsuma Women's University, 12 Sanban-cho, Chiyoda-ku, Tokyo 102-8357, Japan*
[15]*National Astronomical Research Institute of Thailand (Public Organization), 260 Moo 4, T. Donkaew, A. Maerim, Chiang Mai 50180, Thailand*
[16]*Mizusawa VLBI Observatory, National Astronomical Observatory of Japan, 2-21-1 Osawa, Mitaka, Tokyo 181-8588, Japan*

Accepted 2024 December 16. Received 2024 November 30; in original form 2024 April 21

ABSTRACT

We confirmed the existence of a massive protocluster in G23.43−0.18 from our Atacama Large Millimeter/submillimeter Array (ALMA) 1.3 mm continuum and molecular line observations. We resolved the region into one main massive protostellar object, G23.43−0.18 A, one intermediate mass protostellar object, G23.43−0.18 B, and three low mass objects, G23.43−0.18 C1, G23.43−0.18 C2, and G23.43−0.18 C3. A spiral arm structure is observed in G23.43−0.18 B. G23.43−0.18 A 1.3 mm dust continuum emission showed a 'butterfly' morphology with clear evidence of the existence of a cavity and bipolar outflow with an inclination angle of 50°. G23.43−0.18 B presents a compact rotating structure, and possibly an inner Keplerian disc, traced with methanol lines and powers a jet revealed by multiple compact emission peaks in CO, indicating episodic ejections every 300 yr. The presence of 6.7 GHz methanol masers in G23.43−0.18 A and G23.43−0.18 B are strong indications that both objects host massive protostars and are good sites to test some theories of the early evolutionary phases of massive stars.

Key words: masers – techniques: interferometric – stars: formation – ISM: individual objects: G23.43−0.18 A – submillimetre: ISM.

1 INTRODUCTION

The impacts of high-mass stars to their natal environment are enormous. Radiation pressure (Tanaka, Tan & Zhang 2017), accretion bursts (Caratti o Garatti et al. 2017; Hunter et al. 2017; Liu et al. 2018; Brogan et al. 2019; Burns et al. 2020), jets (Torrelles et al. 1996), outflows (Chibueze et al. 2012), and supernovae (Rogers & Pittard 2013) are some of the way massive stars feedback into their surroundings. Recent observational studies of the evolution of massive stars have provided additional clues into the rather mysterious processes leading to the birth of massive stars.

Accretion bursts (Caratti o Garatti et al. 2017; Burns et al. 2020), spiraling accretion flow, and disc fragmentation (Liu et al. 2015, 2019; Ilee et al. 2018; Johnston et al. 2020) are some of the newly unveiled mechanisms associated with the formation of high-mass stars. Substructures and fragments are becoming common features of discs of massive protostars, some of which have been confirmed to be in Keplerian motions (Johnston et al. 2015, 2020; Ilee et al. 2016; Beuther et al. 2017; Maud et al. 2019). The range of separation between the protostars and disc fragments reported so far is ∼1000 to ∼2000 au. Accretion of fragments has been used to explain accretion bursts in massive protostars like G358.93−0.03 (Sugiyama et al. 2019; Chen et al. 2020; Meyer et al. 2017, 2018). André Oliva & Kuiper (2020) investigated the early evolution of a fragmented disc around a massive protostellar object using a high-resolution

★ E-mail: chibujo@unisa.ac.za, james.chibueze@gmail.com

Table 1. ALMA observation details.

Parameter	Cycle 3
Project code	2015.1.01571.S
Date	2016 August 15, 19, and 22
Number of antennas	38, 39, 40 (12 m array)
Baseline length	15.1 m–1.5 km
Amplitude calibrator	J1733−1304 or J1924−2914
Bandpass calibrator	J1751+0939
Phase calibrator	J1851+0035
SPW0	212.88 GHz–213.81 GHz (969.24 kHz spectral resolution)
SPW1	216.55 GHz–217.49 GHz (969.24 kHz spectral resolution)
SPW2	229.44 GHz–229.91 GHz (969.24 kHz spectral resolution)
SPW3	230.22 GHz–230.68 GHz (969.24 kHz spectral resolution)
SPW4	231.34 GHz–232.28 GHz (969.24 kHz spectral resolution)
Velocity resolution	1.27–1.38 km s^{-1}
Typical rms	1.5 mJy beam^{-1} (line), 0.1 mJy beam^{-1} (continuum)
Continuum beam-size	0.27 arcsec × 0.24 arcsec [P.A. −86.5°] (at 222.58 GHz centre frequency)
$^{12}CO_{v=0}(J = 2 - 1)$	230.53800 GHz
$SiO_{v=0}(J = 5 - 4)$	217.10498 GHz
CH_3OH transitions	213.427 ($1_{1,0} - 0_{0,0}$), 216.946 ($5_{-1,4} - 4_{-2,3}$), 217.299 ($6_{1,5} - 7_{2,5}$), 229.589 ($15_{-4,11} - 16_{-3,14}$), 229.758 ($8_{1,8} - 7_{-0,7}$), 230.368 GHz ($22_{4,18} - 21_{5,17}$)

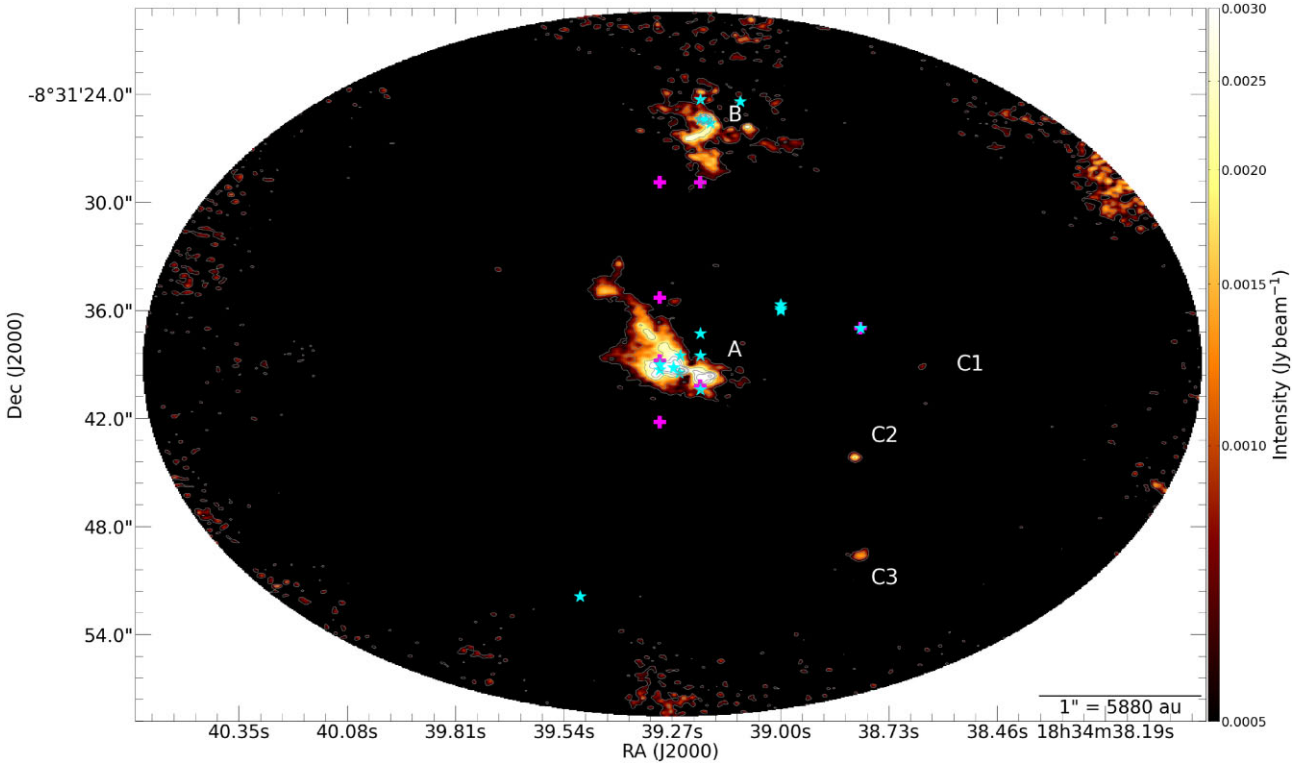

Figure 1. Primary beam corrected 1.3 mm dust continuum image of G23.43−0.18. The contour levels are [0.5, 1, 2, 3, 4] mJy beam^{-1} with an rms of 0.12 mJy beam^{-1}. The positions of the 6.7 GHz CH_3OH masers are indicated by stars, while crosses indicate the positions of the 22 GHz H_2O masers. As shown in the bottom right of this figure, 1 arcsec corresponds to a linear scale of 5880 au at 5.88 kpc.

self-gravity-radiation hydrodynamical simulation. Their simulation showed, among other things, that a massive young stellar object (MYSO) is formed in the centre of its collapsed cloud surrounded by a fragmenting Keplerian-like accretion disc with spiral arms. Gravitational instabilities caused the formation of spiral arms and fragments inside the disc.

Rotating outflows such as those observed in Orion source I (Hirota et al. 2017) help expel angular momentum from the MYSO into its environment and could create a cavity along their paths. Kuiper, Yorke & Turner (2015) and Kuiper, Turner & Yorke (2016) described the three main effects of a protostellar outflow, namely; (i) decrease in accretion flow towards the protostar due to the redirection of some of the accretion flow; (ii) contribution of outward directed momentum that impedes infall on to the forming protostar; and (iii) production of low-density bipolar cavity plowed by the outflowing material. Outflows play a significant role in the formation of massive stars

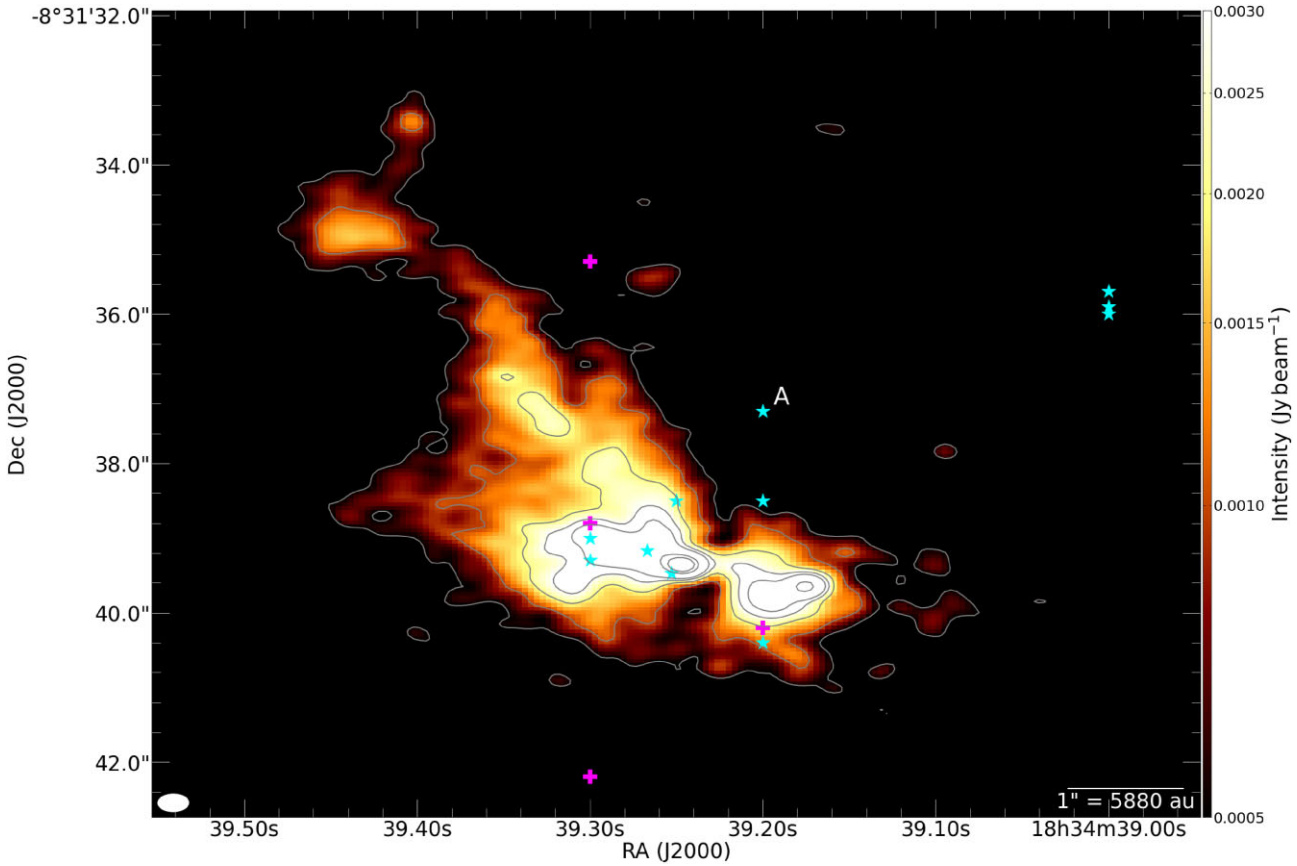

Figure 2. Zoom-in of the 1.3 mm dust continuum emission of G23.43−0.18 A. The contour levels, stars, and crosses are the same as in Fig. 1. White ellipse at the bottom left is the ALMA synthesized beam.

and also drive their feedback into their surroundings. Two kinds of outflows are typically associated with YSOs, a fast $v \sim 100$–1000 km s^{-1} collimated jet as well as a slower wide-angle molecular outflow $v \sim 1$–30 km s^{-1} (Frank et al. 2014).

G23.43−0.18 is a massive star-forming region located at a parallax distance of $5.88^{+1.37}_{-0.93}$ kpc (Brunthaler et al. 2009). It is associated with 6.7 GHz methanol masers which are known to be exclusively associated with massive star-forming regions (Fujisawa et al. 2014; Hu et al. 2016). The dust clump hosting this massive star-forming region is reported in the APEX (Atacama Pathfinder Experiment) Telescope Large Area Survey of the Galaxy (ATLASGAL) survey to have a dust temperature of 24.6 ± 0.6 K, a luminosity, $L_{\rm bol}$ of 1235.6 $L_\odot$, an envelope mass of 63 $M_\odot$ (Contreras et al. 2013), and is associated to molecular line emission like ^{13}CO ($J = 1 - 0$) and CS ($J = 2 - 1$) (Kim & Koo 2003; Walsh et al. 1998, 2003). Wood & Churchwell (1989) reported the detection of an ultra-compact H II (UCHII) region at 6 cm with the very large array (VLA) near G23.43−0.18 , although the UCHII is 7 arcmin to the north–east of the region, outside of the field of view of our observations. G23.43−0.18 is associated with a number of maser species including Class I and II CH_3OH, H_2O, and OH masers (Palagi et al. 1993; Caswell et al. 1995; Slysh et al. 1999; Kang et al. 2016; Beuther et al. 2019). Dempsey, Thomas & Currie (2013) reported the $V_{\rm LSR}$ of G23.43−0.18 to be 104.5 km s^{-1} based on their ^{12}CO (3–2) James Clark Maxwell Telescope (JCMT) observations. However, Shirley et al. (2013) measured the $V_{\rm LSR}$ as 101.9 km s^{-1} with N_2H^+(3–2) observed with the Heinrich Hertz Submillimeter Telescope. Using ALMA 216.946 GHz CH_3OH line observations, we derived the $V_{\rm LSR}$ to be 102.1 km s^{-1}. This value is adopted in this paper.

In this paper, we will report the results of our high-resolution Atacama Large Millimeter/submillimeter Array (ALMA) observations of G23.43−0.18. A spiral arm, rotating structures, outflows and their associated cavity, and possible jet systems observed inside the cores of the region are discussed. This study forms part of our Korean VLBI (very long baseline interferometry) Network (KVN) and VLBI Exploration of Radio Astrometry (VERA) array, KVN and VERA Array (KaVA), star formation large programme[1] to study massive protostellar objects associated with masers (Kim et al. 2018, 2020).

2 OBSERVATIONS, DATA CALIBRATION, AND IMAGING

Our ALMA band 6 observations of G23.43−0.18 were carried out on 2016 August 15, 19, and 22 (project 2015.1.0171.S: P.I. M.-K. Kim) as part of the KaVA star formation large project. We report on the observations of August 15 in this work. We set five spectral windows (spws) to cover the ^{12}CO, SiO (5−4), and multiple transitions of CH_3OH lines as well as 1.3 mm continuum emission. The data calibration was carried out using the ALMA pipeline in the CASA version 4.7 package (McMullin et al. 2007). The half-power beam-width (HPBW) of the primary beam is approximately 27 arcsec at the

[1] https://radio.kasi.re.kr/kava/large_programs.php#sh3

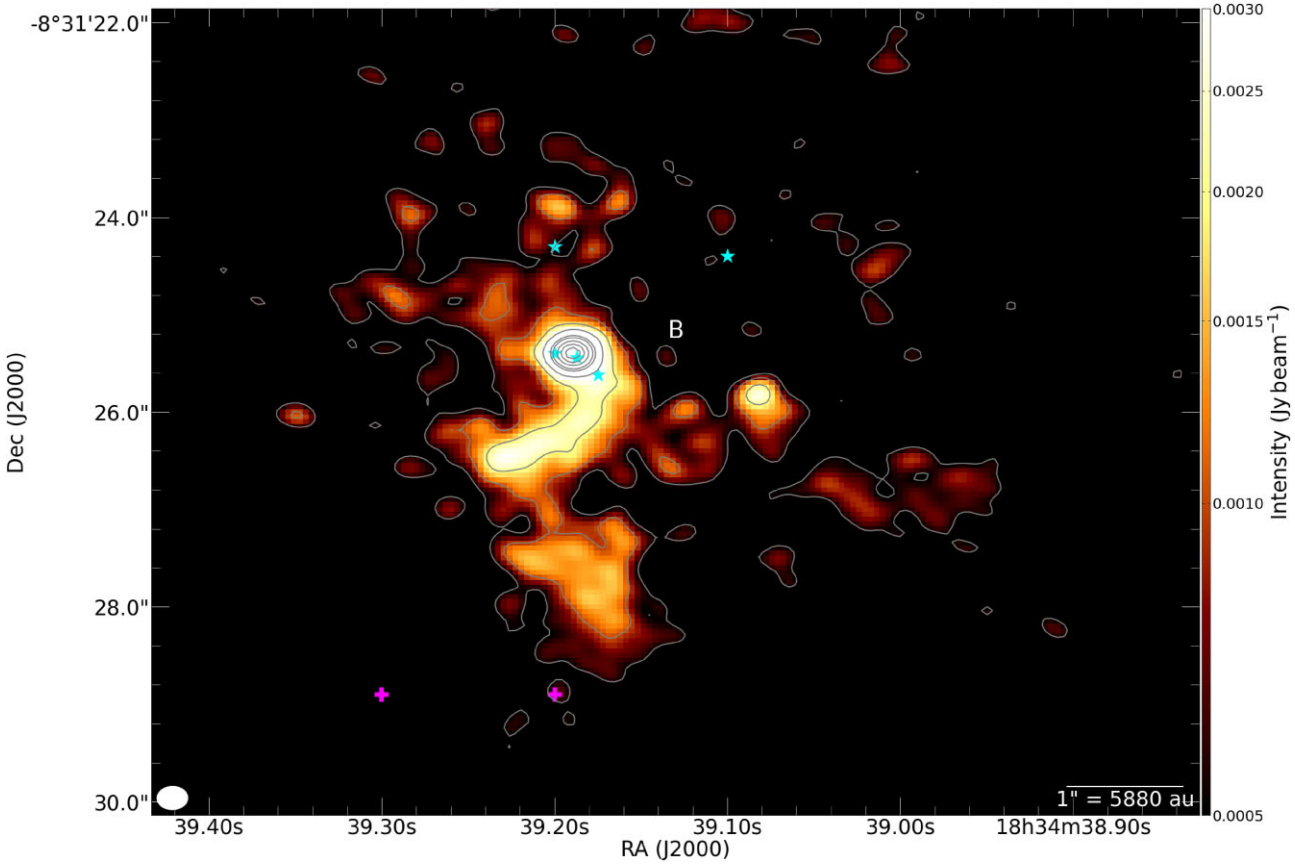

Figure 3. Zoom-in of the 1.3 mm dust continuum emission of G23.43−0.18 B. The contour levels, stars, and crosses are the same as in Fig. 1. White ellipse is the same as in Fig. 2.

observing frequencies; the synthesized beam size of the continuum data was 0.27 arcsec × 0.24 arcsec, while for the line images it ranges from 0.25 arcsec × 0.26 arcsec to 0.30 arcsec × 0.26 arcsec using a robust weighting of 0.5. More details of the observations are presented in Table 1, see also Kim et al. (2020).

3 RESULTS

3.1 G23.43−0.18 1.3 mm continuum emission

Sources of dust continuum emission at 1.3 mm were detected in the centre (labelled as A in Figs 1 and 2), to the north (labelled as B in Figs 1 and 3) and to the south-west (labelled as C in Figs 1 and 4) of the phase tracking centre of G23.43−0.18. Figs 1, 2, 3, and 4 show the dust continuum emission (with zoom-ins) of the core in G23.43−0.18.

G23.43−0.18 A: This central dust continuum source (see Fig. 2) showed a bright 1.3 mm emission extending over 7.5 arcsec (corresponding to 44 000 au) from the north-eastern tip of the emission to the south-western tip. The integrated flux of G23.43−0.18 A is 0.2 Jy, and the peak intensity is 12.1 mJy beam^{-1} at $(\alpha, \delta) = (18^{h}34^{m}39\overset{s}{.}249, -08^{\circ}31'39\overset{''}{.}34)$. The most prominent feature of the morphology of G23.43−0.18 A is the 'butterfly' shape structure with a slightly inclined north–south cavity near the peak of the continuum emission. Excluding the weak north-east spur of G23.43−0.18 A, the butterfly shape covers 4.6 arcsec or 27 000 au. The central cavity splits the main continuum core into east and west components. G23.43−0.18 A is associated with a number of 6.7 GHz CH_3OH and 22 GHz H_2O masers. The 6.7 GHz CH_3OH masers were observed with the Australia Telescope Compact Array (Caswell 2009; Breen et al. 2015), Parkes Observatory 64-m telescope (Caswell et al. 1995; Breen et al. 2015), Hartebeesthoek 26-m telescope (Goedhart, Gaylard & van der Walt 2004), Hitachi and Takahagi 32-m telescopes (Yonekura et al. 2016), Green Bank Telescope (Menten 1991), Torun 32-m telescope (Szymczak et al. 2002, 2012), Effelsberg 100-m telescope (Vlemmings, Torres & Dodson 2011), and Shanghai Tianma 65-m Telescope (Yang et al. 2019). The 22 GHz H_2O masers observations were carried out with the Very Large Array (Forster & Caswell 1989, 1999), Australia Telescope Compact Array (Cesaroni et al. 1988; Breen & Ellingsen 2011), Medicina 32-m telescope (Palagi et al. 1993; Valdettaro et al. 2001), Effelsberg 100-m telescope (Szymczak, Pillai & Menten 2005), Green Bank Telescope (Hogge et al. 2018), and Nanshan 25-m telescope (Xi et al. 2015).

G23.43−0.18 A also shows some blobby structures. In molecular line emission, we see a clear NW–SE molecular outflow, both in SiO, Fig. 5 as well as in ^{12}CO ($J = 2 - 1$) (Figs 6, 7 and 8). Fig. 5 shows the SiO ($J = 5 - 4$) channel maps superimposed on 1.3 mm contours of G23.43−0.18 A. The SiO emission centred on the continuum cavity is clear, as well as an 'X' shape in the last few channel maps (106.7−99.9 km s^{-1}). Figs 6 and 7 show the blue and redshifted channel maps, respectively of the ^{12}CO ($J = 2 - 1$) emission. The 'X' shape traced in SiO on a smaller scale can clearly be seen in both figures on a larger scale. Fig. 8 shows the blue and red lobes of the molecular outflow traced in ^{12}CO ($J = 2 - 1$). The cavity seen in the moment maps is clear, as well as an 'S' shape passing through the continuum core. Fig. 8 also contains a zoomed image of the centre

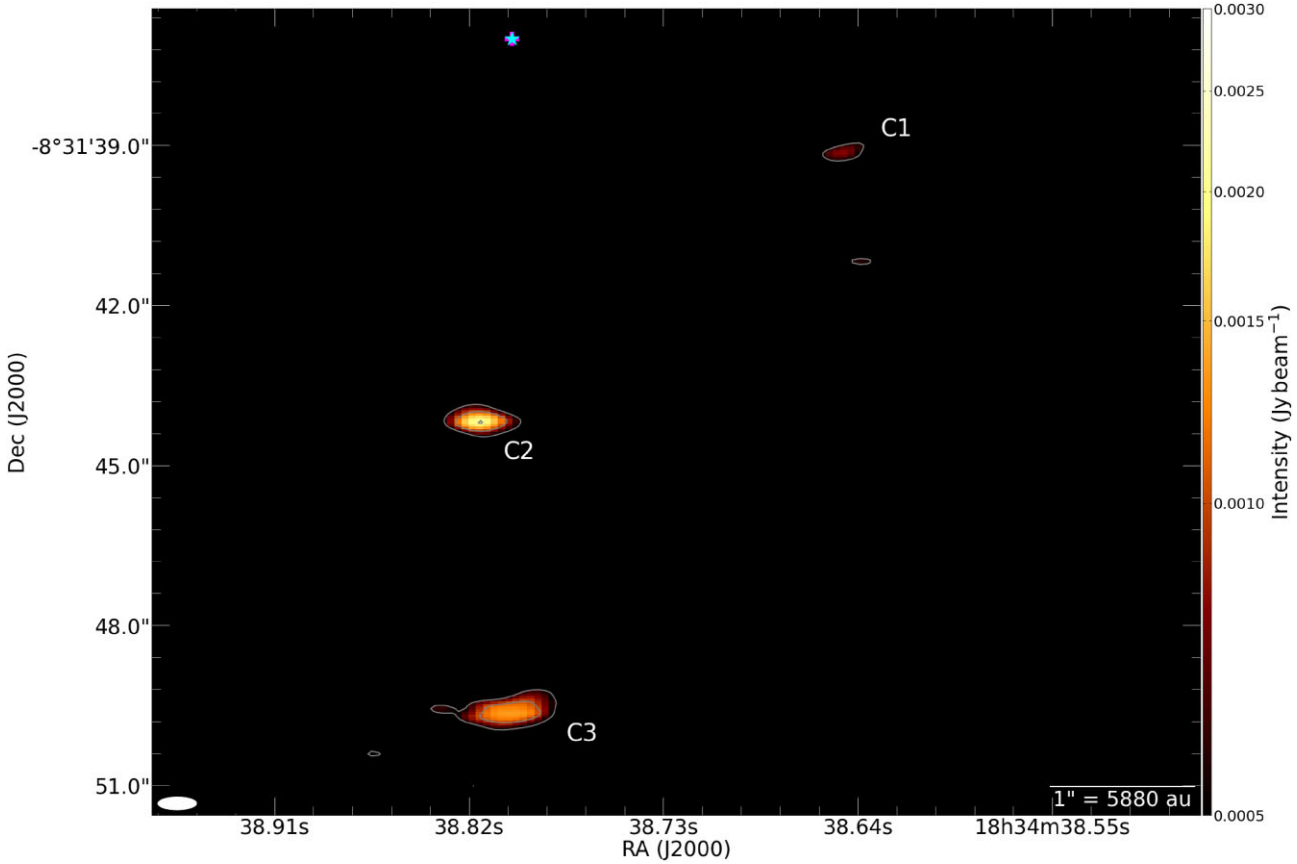

Figure 4. Zoom-in of the 1.3 mm dust continuum emission from C1, C2, and C3 cores. The contour levels, star, and cross are the same as in Fig. 1. White ellipse is the same as in Fig. 2.

of G23.43−0.18 A. The ^{12}CO ($J = 2 - 1$) emission moment 0 map shows two bow shapes, separated by a distance of 26000 au.

G23.43−0.18 B: The northern dust continuum emission comprise of a 1600 au compact continuum core (see Fig. 3) with a peak intensity of 23.5 mJy beam^{-1} at (α, δ) = ($18^h34^m39\overset{s}{.}189$, $-08°31'25\overset{''}{.}41$), and an integrated flux of 26.3 mJy. G23.43−0.18 B is only 6 arcsec from the edge of the ALMA primary beam. However, we achieved enough sensitivity to detect faint structures of continuum emission around the main core. A clear spiral arm structure extending southward from the main G23.43−0.18 B core is detected. This spiral arm structure is stretched out through an angular scale of 1.6 arcsec from the continuum peak to the end of the spiral, corresponding to 9400 au. Some of the 6.7 GHz CH_3OH masers are located near the continuum peak emission of G23.43−0.18 B, which could be an indication that the protostar is massive.

G23.43−0.18 C: There are three other compact continuum cores labelled as C1, C2, and C3 (see Fig. 4) detected in the south-western region of G23.43−0.18. C1 is the faintest of the three with an integrated flux of 1.6 mJy, and a peak intensity of 0.8 mJy beam^{-1} at (α, δ) = ($18^h34^m38\overset{s}{.}647$, $-08°31'39\overset{''}{.}14$). C2 is marginally resolved in our observations with an integrated flux of 3.2 mJy, and a peak intensity of 1.8 mJy beam^{-1} at (α, δ) = ($18^h34^m38\overset{s}{.}815$, $-08°31'44\overset{''}{.}17$). C3 is 5.5 arcsec south of C2 and has an integrated flux of 10.4 mJy, and a peak intensity of 1.7 mJy beam^{-1} at (α, δ) = ($18^h34^m38\overset{s}{.}801$, $-08°31'49\overset{''}{.}62$). The ^{12}CO emission, particularly at the redshifted velocities, reveals outflows emerging from C1 and C3 cores (see Fig. 7 and also Fig. 8a). This is an indication that the cores are actively undergoing star formation, though in earliest stage, as evident from lack of complex molecule line emission.

4 DISCUSSIONS

4.1 Estimates of the gas masses and column densities of the dust cores

We took advantage of the sensitivity of millimeter observation to the circum-(proto)stellar material to estimate the gas masses of the cores of G23.43−0.18 following the methods in Brogan et al. (2009).

$$M_{\rm gas} = \frac{3.24 \times 10^{-3}\, S_\nu({\rm Jy})\, D^2({\rm kpc})\, R\, C_{\tau_{\rm dust}}}{J(\nu, T_{\rm dust})\, \nu^3({\rm THz})\, \kappa_\nu}\, {\rm M}_\odot, \quad (1)$$

where S_ν is the integrated flux density of the core, R is the ratio of gas to dust (100), $J(\nu, T_{\rm dust}) = 1/(exp(h\nu/T_{\rm dust}k) - 1)$, k and h are the Boltzmann and Planck's constants, respectively, and $C_{\tau_{\rm dust}} = \tau_{\rm dust}/(1 - e^{-\tau_{\rm dust}})$ is the correction factor for the dust opacity. We adopted a dust opacity, κ_ν of 1 cm^2 g^{-1} (Ossenkopf & Henning 1994) up to a maximum of 50 K. The excitation temperatures (see Fig. 9a and b) of CH_3OH in G23.43−0.18 A and G23.43−0.18 B were calculated under the assumption of local thermodynamic equilibrium (Goldsmith & Langer 1999) and used as the dust temperatures, $T_{\rm dust}$.

Goldsmith & Langer (1999) rotation diagram method employs different transitions of the same molecule that span over a range of energies in estimating the temperatures, which can be inferred from

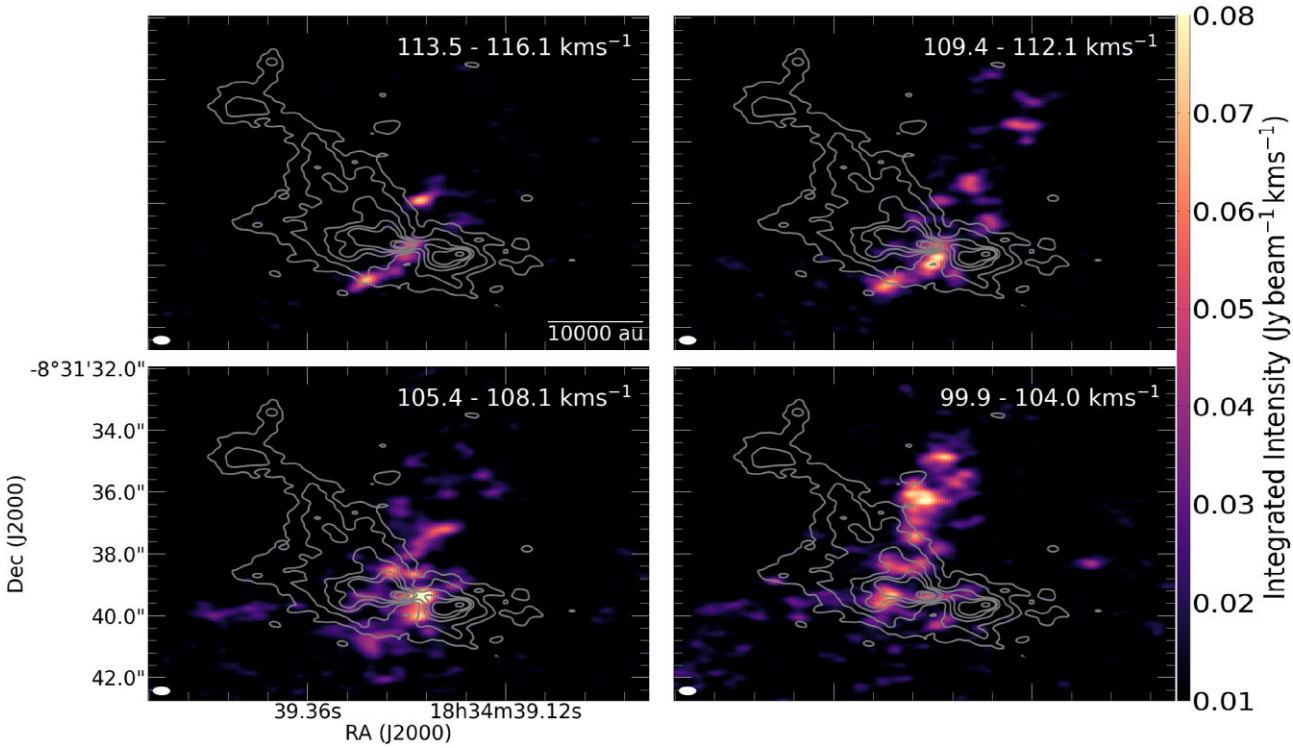

Figure 5. Primary beam corrected SiO ($J = 5 - 4$) line integrated emission showing the shocked gas of G23.43−0.18 A due to the bipolar outflow along the axis of the observed dust cavity, with a typical rms of 2.2 mJybeam^{-1}. The white contours represent the 1.3 mm dust continuum emission. The contour levels and white ellipse are the same as in Fig. 2.

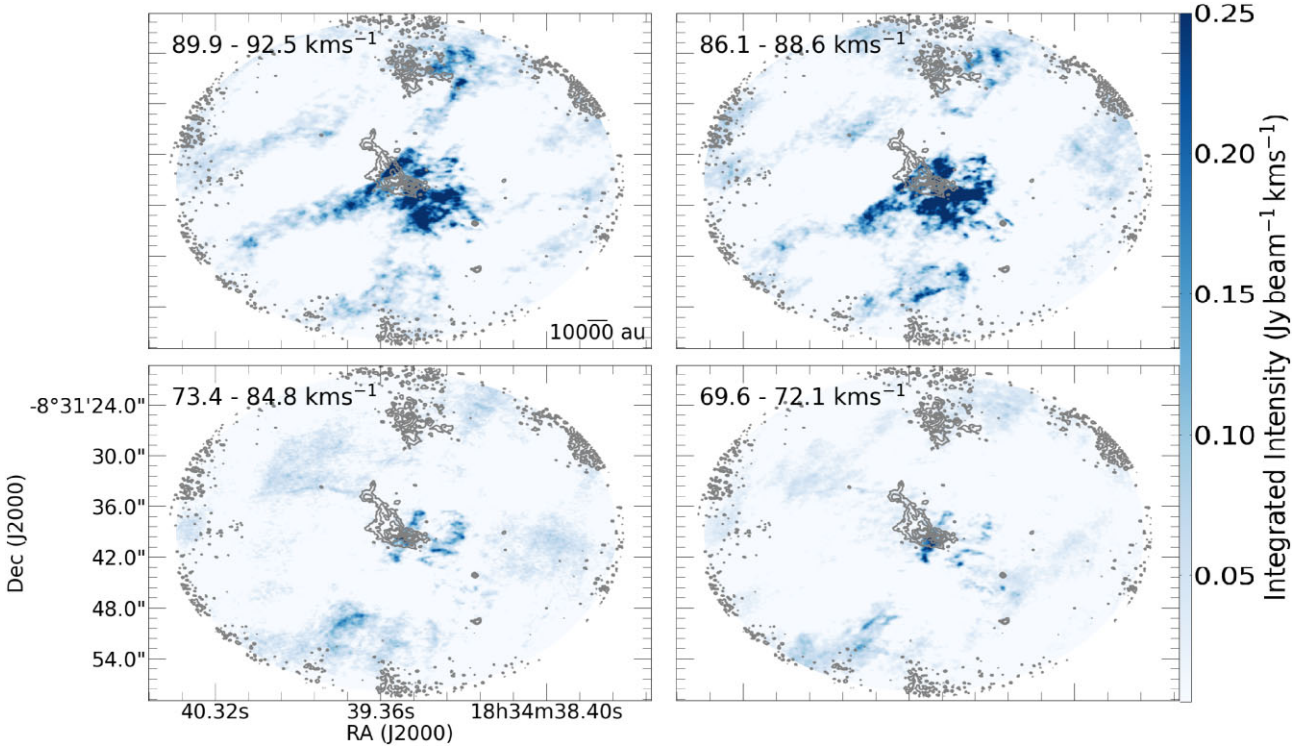

Figure 6. ^{12}CO ($J = 2 - 1$) integrated blueshifted emission. The grey contours represent the 1.3 mm dust continuum emission. The contour levels are the same as in Fig. 1.

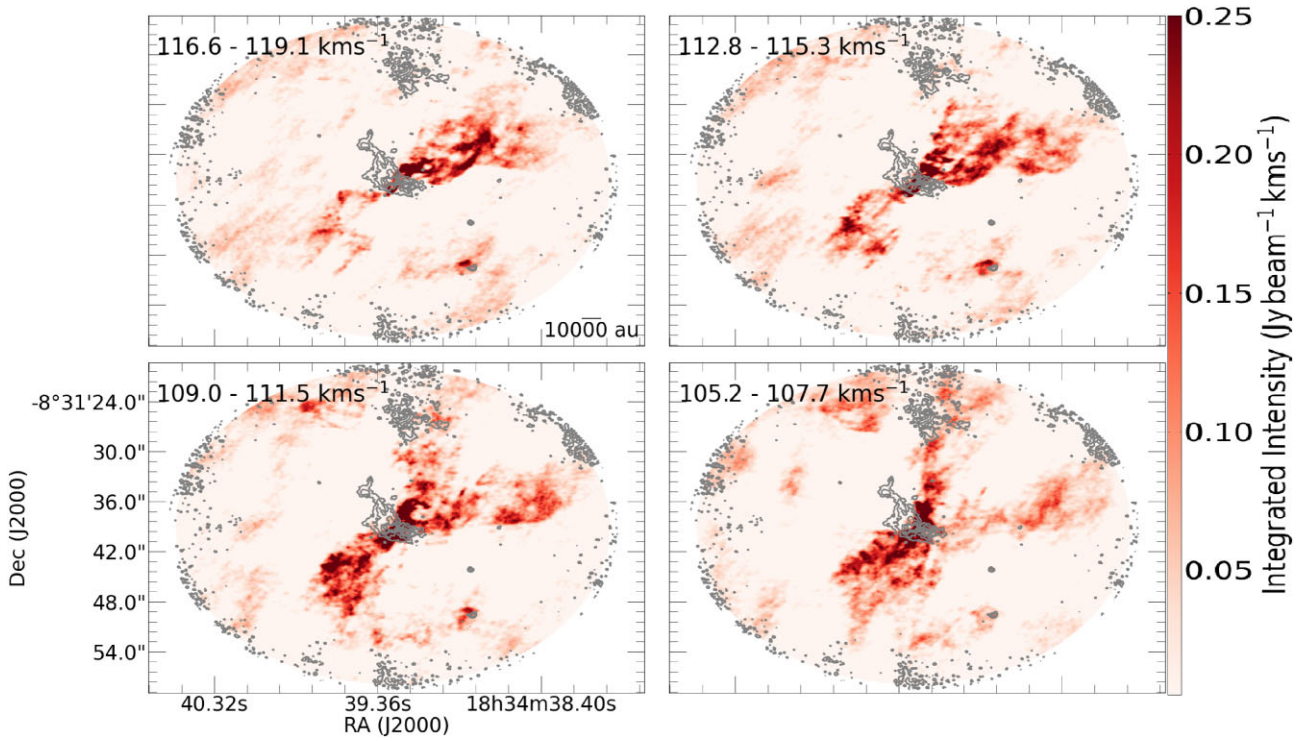

Figure 7. ^{12}CO ($J = 2 - 1$) integrated redshifted emission. The grey contours represent the 1.3 mm dust continuum emission. The contour levels are the same as in Fig. 1.

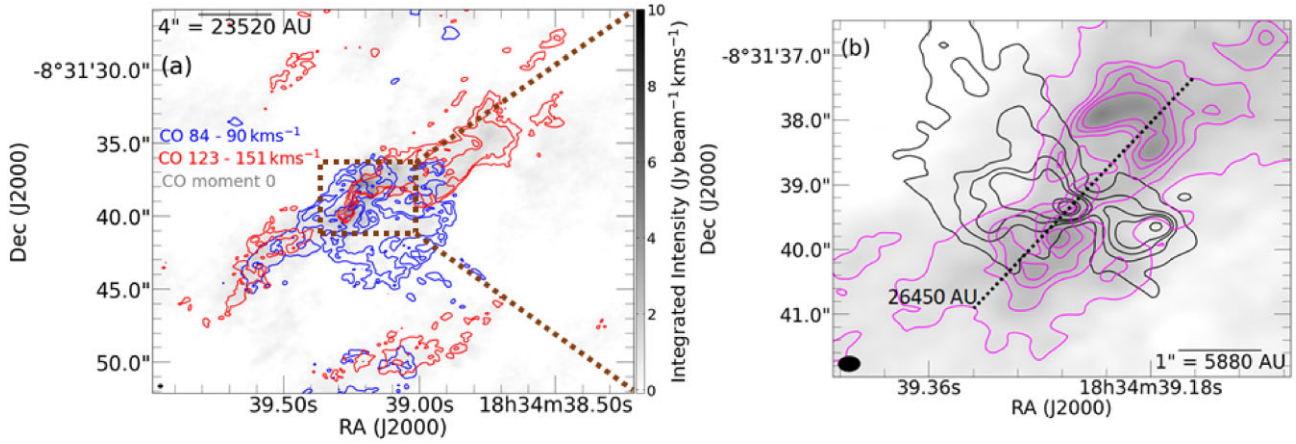

Figure 8. ^{12}CO ($J = 2 - 1$) integrated intensities of outflow originating in G23-A. (a) Blueshifted and redshifted outflow lobes with contour levels 175 mJy·km s^{-1} ×[1, 2] superimposed on ^{12}CO ($J = 2 - 1$) moment 0 map integrated over {85 − 88, 100 − 140} km s^{-1} (greyscale). (b) Zoomed in on G23-A. The greyscale is the same as (a), the magenta contours show the moment zero contours with levels of 1 Jy·km s^{-1} × [1, 2, 2.5, 3, 3.5], the black contours is the 1.3 mm continuum emission at levels = [1, 2, 3, 4] mJy beam^{-1} with an rms of 0.12 mJy beam^{-1}. The black dotted line and text shows the extent of the bow structure. The linear scale of (a) and (b) are on the top left and bottom right, respectively.

this relations

$$\frac{N_u}{g_u} = \frac{3k}{8\pi^3 \nu g_I g_K} \frac{1}{\mu^2 S} \int S_\nu \mathrm{d}v \tag{2}$$

and

$$\log(N_u/g_u) = \log(N_{\rm tot}/Q(T_{\rm rot})) - 0.4343 E_u/kT_{\rm rot}, \tag{3}$$

where k is Boltzmann's constant, ν is the frequency, g_I and g_K are the degeneracies associated with the nuclear spin, and k quantum number, respectively, μ^2 is the square of the dipole matrix element, S is the statistical line strength, $\int S_\nu \mathrm{d}v$ is the observed integrated intensity of the transition, $N_{\rm tot}$ is the total column density, $Q(T_{\rm rot})$ is the partition function evaluated at the rotation temperature $T_{\rm rot}$, and E_u is the upper state energy of the transition. Here, we used CH_3OH transitions J = $1_{(1,0)} - 0_{(0,0)}$ at 213.427 GHz, $5_{(-1,4)} - 4_{(-2,3)}$ at 216.946 GHz, $6_{(1,5)} - 7_{(2,5)}$ at 217.299 GHz, $15_{(-4,11)} - 16_{(-3,14)}$ at 229.589 GHz, $8_{(1,8)} - 7_{(-0,7)}$ at 229.758 GHz, and $22_{(4,18)} - 21_{(5,17)}$ at 230.368 GHz. The integrated intensity for each transition was calculated from Gaussian fits to the line emission at the continuum

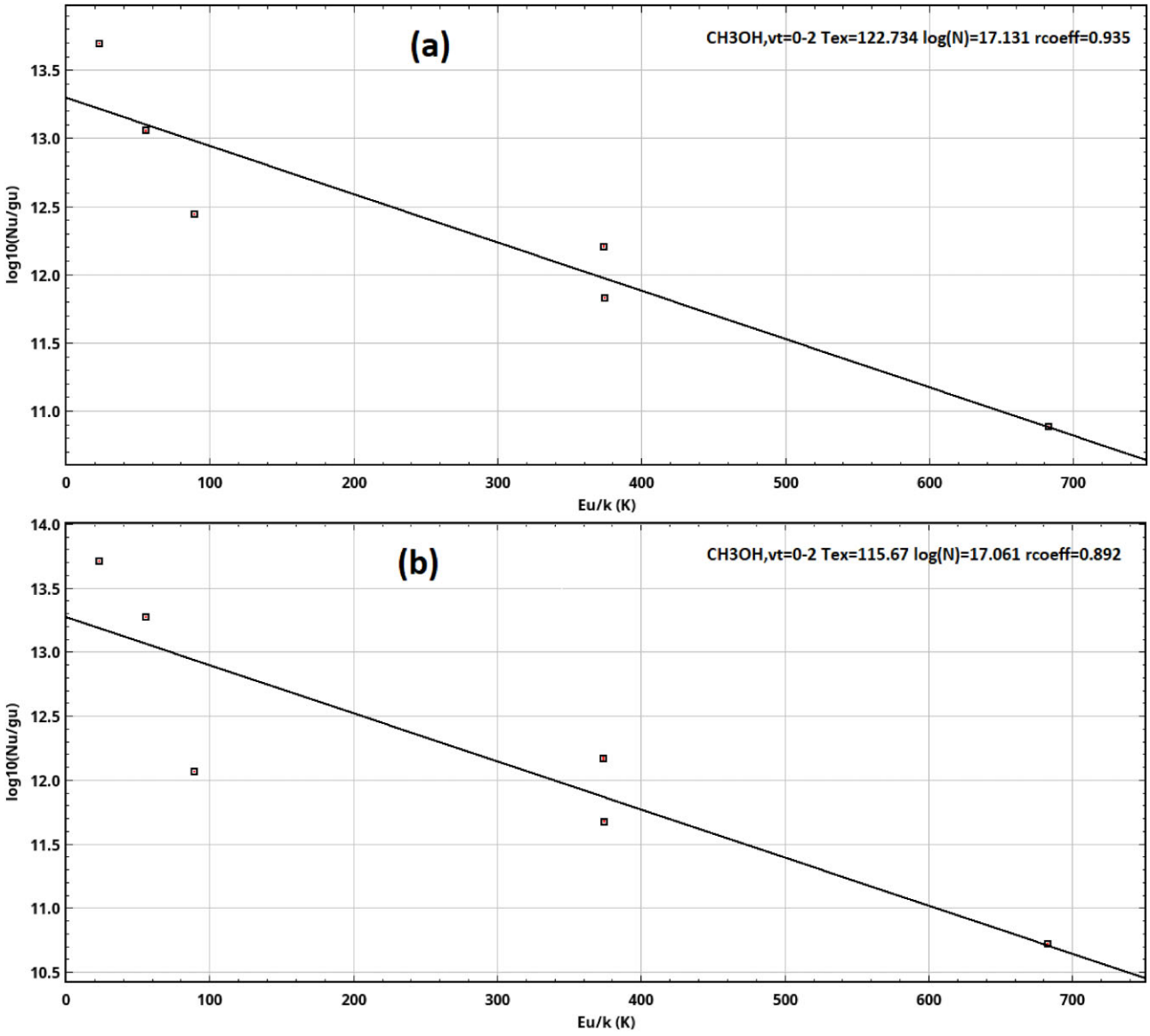

Figure 9. Rotational temperature diagram of CH_3OH in (a) G23.43−0.18 A and (b) G23.43−0.18 B. The excitation temperature (in units of K), column density (in units of cm^{-2}) and correlation coefficient derived from the analysis are quoted in the upper right corner.

Table 2. Properties of the G23.43−0.18 dust continuum cores extracted from the primary beam corrected image.

Object name	R.A. (J2000) ($^{h\ m\ s}$)	Dec. (J2000) ($^\circ\ '\ ''$)	Peak flux (mJy beam^{-1})	Integrated flux (mJy)	Size (arcsec × arcsec [P.A.] $^\circ$)	T_{dust} (K)	M_{gas} ($M_\odot$)	N_{H_2} (cm^{-2})
G23.43−0.18 A	18 34 39.249	−08 31 39.34	12.1 ± 0.1	203.2 ± 15.0	2.4 × 1.0 [70]	122.7	18.6	2.8×10^{23}
G23.43−0.18 B	18 34 39.189	−08 31 25.41	23.5 ± 2.5	26.3 ± 2.5	0.3 × 0.3 [76]	115.7	2.7	1.3×10^{24}
G23.43−0.18 C1	18 34 38.647	−08 31 39.14	0.8 ± 0.01	1.6 ± 0.01	0.5 × 0.2 [141]	115.7	0.2	5.6×10^{22}
G23.43−0.18 C2	18 34 38.815	−08 31 44.17	1.8 ± 0.02	3.2 ± 0.02	0.4 × 0.3 [21]	115.7	0.3	1.1×10^{23}
G23.43−0.18 C3	18 34 38.801	−08 31 49.62	1.7 ± 0.02	10.4 ± 0.3	0.6 × 0.4 [140]	115.7	1.1	4.0×10^{24}

peaks of G23.43−0.18 A and G23.43−0.18 B. We iteratively solved for the rotation temperature, column density, and optical depth that gives the best χ^2 fit to the data.

The estimated excitation temperature, column density (log N) and average optical depth of CH_3OH lines in G23.43−0.18 A are ∼122.73 K, 17.13 cm^{-2}, and 0.03, respectively, while those of G23.43−0.18 B are ∼115.67 K, 17.06 cm^{-2}, and 0.16, respectively. Due to lack of multiple transitions of CH_3OH in G23.43−0.18 C (C1, C2, and C3) to compute the excitation temperatures, we assumed that of G23.43−0.18 B for their masses and column densities estimation.

The column densities were derived from

$$N_{H_2} = \frac{S_\nu R}{J(\nu, T_{dust})\Omega\kappa_\nu \mu_{H_2} m_H}\ cm^{-2}, \quad (4)$$

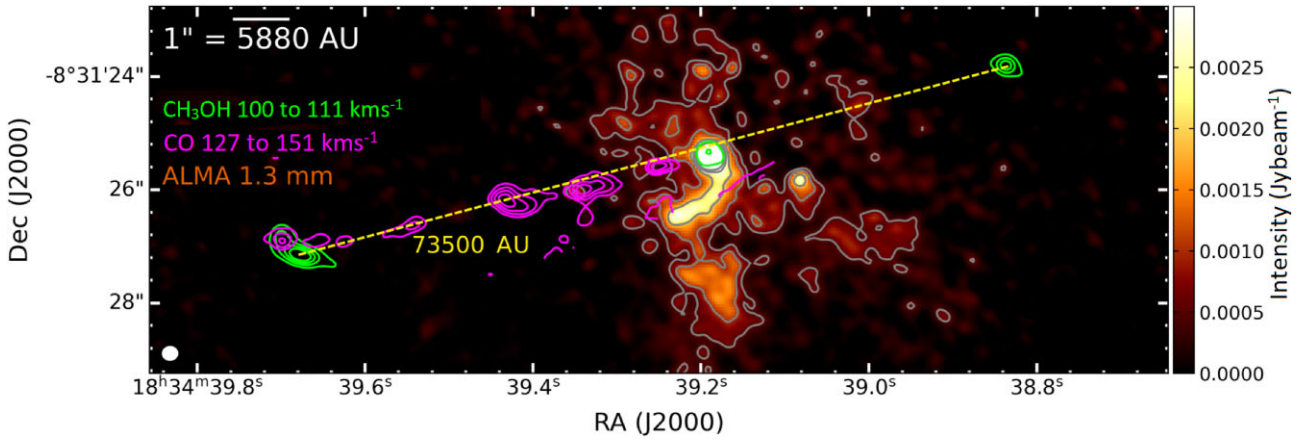

Figure 10. The outflow originating in G23.43−0.18 B. The grey contours and colourscale represent the 1.3 mm dust continuum emission and the contour levels are the same as in Fig. 1. The green contours at levels of 300 mJy·km s^{-1} × [1, 2, 3, 4] show integrated 229.758 GHz CH_3OH molecular line emission, over the velocity range shown in green at the top left. The magenta contours, representing the CO emission, integrated across the shown velocity range in the top left at levels of 25 mJy·km s^{-1} ×[2, 4, 6, 8]. The yellow line shows the length and position angle of the jet.

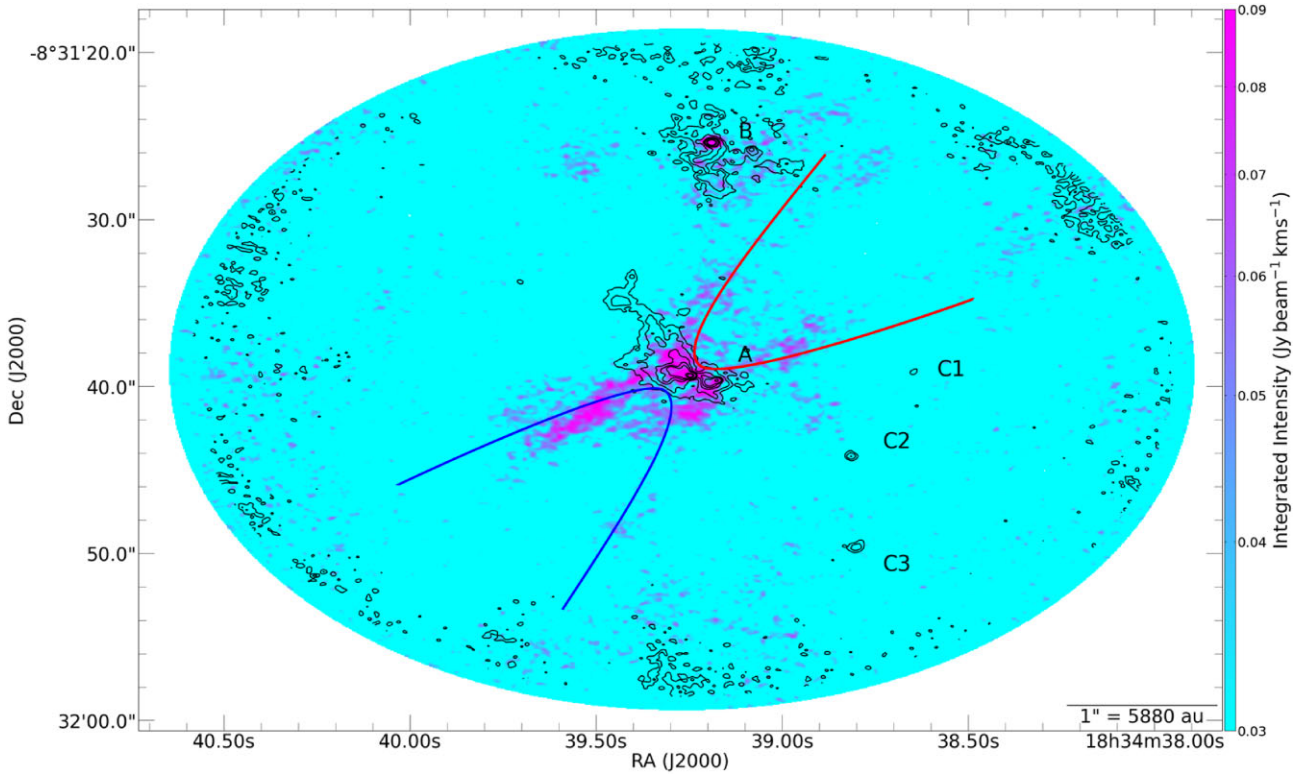

Figure 11. 213.427 GHz CH_3OH line in G23.43−0.18 A tracing the walls of the wide-angle bipolar outflow (indicated with red and blue parabolae) from the protostar. The black contours represent the 1.3 mm dust continuum emission. The contour levels are the same as in Fig. 1.

where Ω is the solid angle of the beam calculated by $\Omega = 1.13 \times \Theta^2$, where Θ is the geometric mean of the beam major and minor axes, μ_{H_2} is the mean molecular weight per hydrogen molecule = 2.8 and m_H is the mass of a hydrogen atom. See Table 2 for derived values of the core gas masses and column densities.

4.2 Cavity and ^{12}CO (2-1) wide-opening angle bipolar outflow in G23.43−0.18 A

A prominent large ^{12}CO ($J = 2 - 1$) bipolar outflow with a wide (∼100°) opening angle and angular size of ≥20 arcsec was detected towards G23.43−0.18 A as is seen in Figs 6 and 7. The outflow aligns

with the axis of the observed dust cavity. The east–west angular size of the north–south cavity observed in G23.43−0.18 A is ∼0.4 arcsec, a linear size of 2350 au. The north–south axis of the cavity aligns with the axes of the wide-opening angle ^{12}CO ($J = 2 - 1$) outflow and the collimated SiO bipolar outflow (see Fig. 5). We estimated the inclination angle θ of the wide-angle molecular outflow by first convolving the redshifted and blueshifted ^{12}CO ($J = 2 - 1$) maps of Fig. 8 (a) with a 2 arcsec × 2 arcsec beam, and then using the method of Kong & Wu (2011) on the small scale bow structure in Fig. 8 (b). This method can only be used for a conical-like outflow in which the driving source is symmetrically centred along the outflow lobes. The method depends mainly on the accurate location of the driving source. In our calculation, we chose the continuum peak position of G23.43−0.18 A as the driving source and derived an inclination angle of 50° for the G23.43−0.18 A outflow, which is half-way between the sky and the line of sight. The inclination angle is determined with respect to the plane of the sky.

Rosen & Krumholz (2020) suggested momentum injection by outflows and radiation pressure as key drivers of excavation of cavities in protostars. According to Kuiper et al. (2016), the momentum of the outflows entrain and eject 20–50 per cent of gas in dense cores. Cunningham et al. (2011) found that there is a lower disc surface density threshold which determines how likely a protostellar clump is to form high-mass stars. Further, they found that an outflow raises the surface density threshold, further diminishing high mass star formation efficiency.

We used the method of Tanabe et al. (2019) to derive the parameters for the wide angle bipolar outflow: the ^{12}CO outflow mass, outflow momentum, outflow energy, outflow dynamical time, mass outflow rate, outflow momentum flux, and energy ejection rate. The outflow mass, $M_{\rm outflow}$ is calculated from:

$$M_{\rm outflow} = \sum_{|v_{\rm lsr}-v_{\rm sys}|\geq 2\sigma_v} m(v), \tag{5}$$

where $m(v)$ is the mass of each velocity component expressed as:

$$m(v) = 4.33\times10^{13}\,\frac{\bar{\mu}m_{\rm H}}{\chi_{^{12}\rm CO}}\left[\frac{s(v)}{\rm cm^2}\right] f_\tau \left(\frac{T_{\rm ex}}{\rm K}\right)\exp\left(\frac{5.53}{T_{\rm ex}}\right) \times\left[\frac{\overline{T}_{\rm B}(v)}{\rm K}\right]\left(\frac{\Delta v}{\rm Km\,s^{-2}}\right), \tag{6}$$

In equation (6), $\bar{\mu}$ is the mean molecular weight of 2.4, $m_{\rm H}$ is the atomic mass of hydrogen, $\chi_{^{12}\rm CO}$ is the CO abundance taken as 10^{-4} (Frerking, Langer & Wilson 1982), $s(v)$ is the projected area above 3σ level, $f_\tau = \tau_{\rm CO}/(1-e^{-\tau_{\rm CO}})$ is the ^{12}CO correction factor for the optical depth, $\tau_{\rm CO} = -\ln(1-\overline{T}_{\rm B}(v)/T_{\rm ex})$, $T_{\rm ex}$ is the ^{12}CO excitation temperature, $\overline{T}_{\rm B}(v)$ is the averaged brightness temperature of all pixels in $s(v)$, and Δv is the ^{12}CO linewidth. The peak intensity (in Kelvin) of ^{12}CO profile was obtained from Gaussian fitting and adopted as the excitation temperature of ^{12}CO. The projected area $s(v)$ is defined as:

$$s(v) = n_{\rm pix}\left[1.5\times10^{13}\left(\frac{D}{\rm pc}\right)\left(\frac{\Delta\theta}{\rm arcsec}\right)\right]^2\,[\rm cm^2], \tag{7}$$

where $n_{\rm pix}$ is the number of pixels in $s(v)$, D is the distance to the source, and $\Delta\theta$ is the pixel size $= 0\farcs05$. The outflow momentum ($P_{\rm outflow}$) and outflow energy ($E_{\rm outflow}$) are calculated from:

$$P_{\rm outflow} = \sum_{|v_{\rm lsr}-v_{\rm sys}|\geq 2\sigma_v} m(v)|v_{\rm lsr}-v_{\rm sys}| \tag{8}$$

and

$$E_{\rm outflow} = \frac{1}{2}\sum_{|v_{\rm lsr}-v_{\rm sys}|\geq 2\sigma_v} m(v)|v_{\rm lsr}-v_{\rm sys}|^2. \tag{9}$$

The outflow momentum varies with $1/\sin\theta$. Hence, we effectively calculated $P\sin\theta$. The dynamical time-scale of the outflow, $t_{\rm d}$ is derived from:

$$t_{\rm d} = \frac{R_{\rm max}}{\Delta v_{\rm max}}, \tag{10}$$

where $R_{\rm max}$ is the maximum size of the outflow measured in the integrated map and $\Delta v_{\rm max}$ is the maximum velocity of the outflow taken from $|v_{\rm max}-v_{\rm sys}|$, where $v_{\rm max}$ is the highest velocity for emission above 3σ. The mass outflow rate ($\dot{M}_{\rm outflow}$), outflow momentum flux ($\dot{P}_{\rm outflow}$), and energy ejection rate ($\dot{E}_{\rm outflow}$) are obtained from:

$$\dot{M}_{\rm outflow} = \frac{M_{\rm outflow}}{t_{\rm d}}, \tag{11}$$

$$\dot{P}_{\rm outflow} = \frac{P_{\rm outflow}}{t_{\rm d}}, \tag{12}$$

and

$$\dot{E}_{\rm outflow} = \frac{E_{\rm outflow}}{t_{\rm d}}. \tag{13}$$

From these calculations, we found that the average values of the ^{12}CO outflow mass, outflow momentum, outflow energy, outflow dynamical time, mass outflow rate, outflow momentum flux, and energy ejection rate are $\sim 0.72\,\rm M_\odot$, $5.22\,\rm M_\odot$ km s^{-1} , 6.46×10^{44} erg, 1.54×10^4 yr, $4.23\times10^{-5}\,\rm M_\odot\,yr^{-1}$, $3.14\times10^{-4}\,\rm M_\odot$ km s^{-1} yr^{-1} and 1.27×10^{33} erg s^{-1}, respectively.

The derived values are consistent with the largest values obtained in the Orion Molecular Cloud (OMC; Takahashi et al. 2008). Our derived outflow properties are consistent with large scale surveys (de Villiers et al. 2014; Maud et al. 2015) and simulations (Matsushita et al. 2017; Rosen & Krumholz 2020) of molecular outflows originating in high-mass star-forming regions. Our dynamical time-scale limit is in agreement with the t_d derived for most molecular outflows observed in the above-mentioned surveys, where $t_d \sim 10^4 - 10^5$ yr. Our mass estimate should be treated as a lower limit, as the outflow was not fully enclosed within the primary beam which causes an uncertainty in the size of the outflow. Our findings suggest that the driving source of the outflow in G23.43−0.18 A is a massive protostar.

Photoionization have been shown to play a key role as a protostar reaches 10–20 $\rm M_\odot$. Accretion disc shields itself from the impact of photoionization. However, magnetically launched outflows become photoionized forming jet-like UCHII region within the protostar (Tanaka, Tan & Zhang 2016; Kuiper & Hosokawa 2018).

It is important to note that the SiO emission in G23.43−0.18 A in some velocity intervals (Fig. 5) shows high collimation and aligns with the cavity wall pointing to the existence of shocks along the ploughed cavity and the edges of the wide opening angle of the ^{12}CO outflow.

4.3 Possible jet system in G23.43−0.18 B

Fig. 10 shows the possible jet system in G23-B. We detected compact emission of 229.758 GHz CH_3OH thermal line northwest and southeast of G23.43−0.18 B. The northwestern emission is ∼5 arcsec (corresponding to 29400 au) offset from the continuum core, while the southwestern emission is located ∼6 arcsec (corresponding to 35280 au) off from the core. The axis of the two blobs cuts

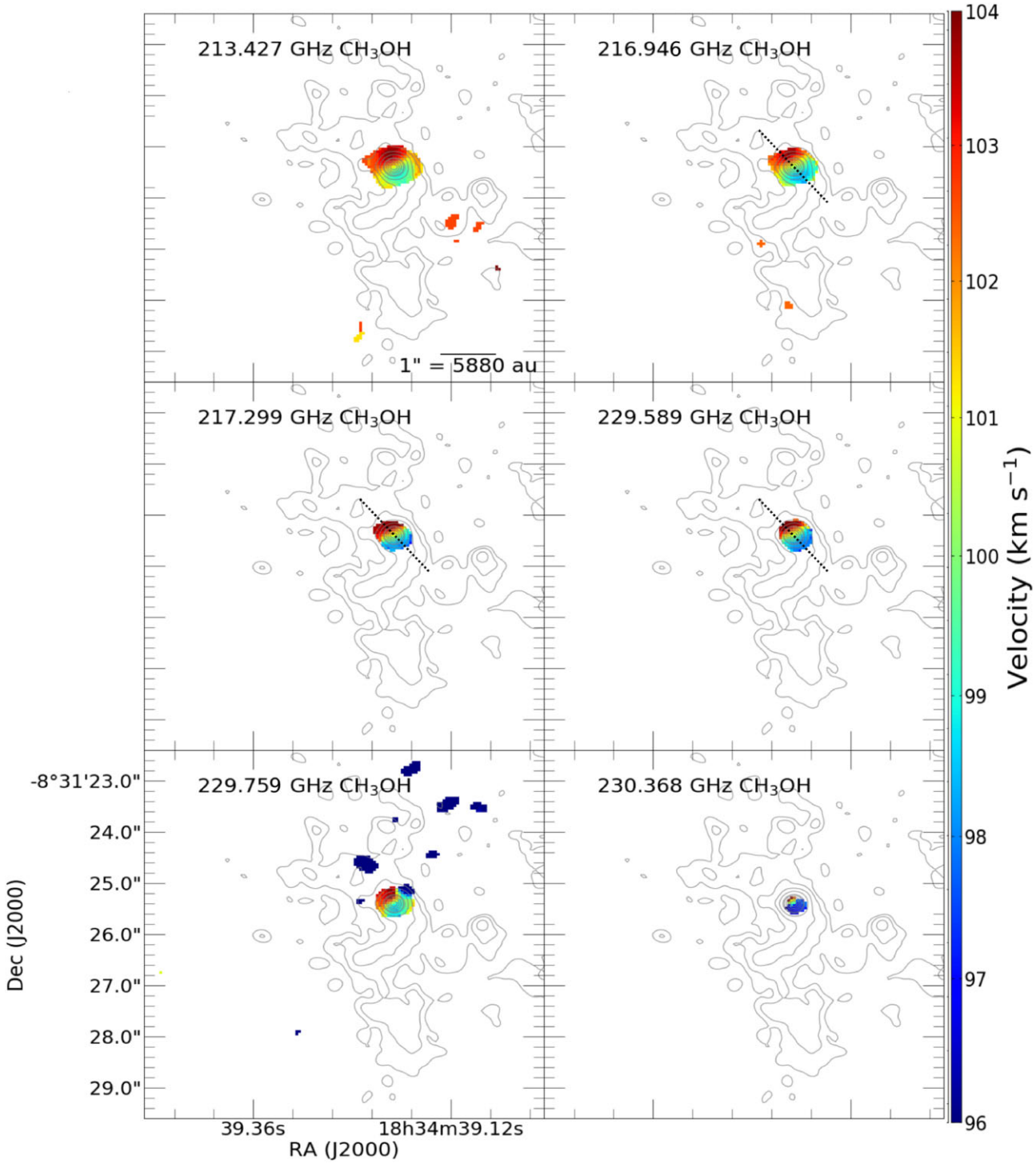

Figure 12. Multiple transitions of CH_3OH lines showing the presence of a rotating structure/disk in G23.43−0.18 B. The grey contours represent the 1.3 mm dust continuum emission and the contour levels are the same as in Fig. 1. Dotted line indicates the line of the constructed PV diagram shown in Fig. 14.

through the G23.43−0.18 B core, thus, confirming it as the driving source of the emission. The CH_3OH emission is only detected in the central region of G23.43−0.18 B and at the edges of the outflow, but not along the rest of the outflow. This is indicative of low column density of CH_3OH along the jet axis, which is suggestive of the existence of a ploughed cavity along the jet. We consider that these compact CH_3OH emissions are tracing shocked environment of a jet launched from the G23.43−0.18 B core, and derived the collimation angle of the jet to be $\sim 19^o$. The presence of a jet confirms active star formation in the region. A highly collimated ^{12}CO outflow is also detected towards G23.43−0.18 B. The presence of knots of emission could be an indication of episodic ejections. Five peaks are visible in CO, which are 1, 2.3, 3.6, 5.3, and 7.7 arcsec corresponding to 5900, 13500, 21700, 31800, and 45200 au

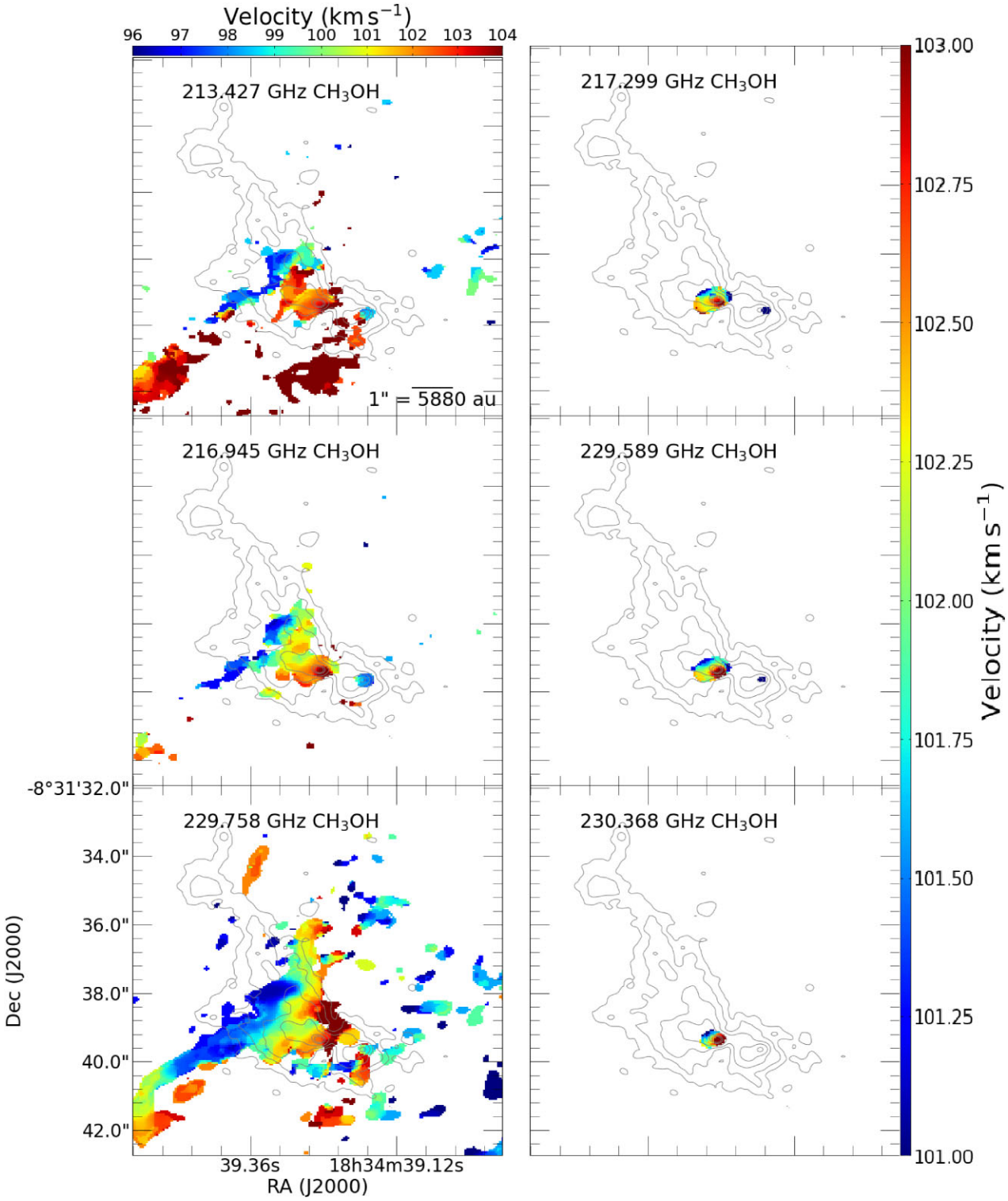

Figure 13. First moment maps of multiple transitions of CH_3OH lines in G23.43−0.18 A. *Left*: velocity field maps from 96 to 104 km s^{-1}. *Right*: velocity field maps from 101 to 103 km s^{-1}. The grey contours represent the 1.3 mm dust continuum emission and the contour levels are the same as in Fig. 1.

from the driving source, respectively. Using the method outlined in Section 4.2, the dynamical time-scales for the knots are 185, 424, 682, 999, and 1420 yr, corresponding to an ejection roughly every 300 yr if these knots are separate ejections. The association of the CO knots with the jet is also witnessed by the fact that their V_{LSR} are up to ∼50 km s^{-1} higher than the systemic velocity of the protostar. This suggests that the knots originate from high velocity episodic ejections/outflow. Knotted structure in protostellar jets and outflows are expected to be seen as a consequence of variable protostellar accretion rates. Examples of this is seen in the

Table 3. Parameter values used to generate Keplerian models with *thindisk* (Maret 2019).

Parameter	Value (Unit)
Distance d	5880 (pc)
Disc intensity I_0	135 (Jy beam^{-1})
Disc FWHM	0.6 (arcsec)
P.A.	55 (deg)
System V_{LSR}	101 (km s^{-1})
Linewidth	3.78 (km s^{-1})
Centrifugal radius r_c	10^5 (au)
Outer radius r_0	1000 (au)
Disc size	10^5 (au)
Stellar mass M_*	variable ($M_\odot$)
Inclination angle i	variable (deg)

simulations by Rosen & Krumholz (2020) in outflows and André Oliva & Kuiper (2020) in discs. Therefore, the knotted structures we see in ^{12}CO emission could indicate episodic accretion in G23.43−0.18 B.

4.4 CH_3OH Lines in G23.43−0.18 and presence of rotating structures

Multiple (213.427, 216.946, 217.299, 229.589, 229.759, and 230.368 GHz) CH_3OH transitions were detected towards G23.43−0.18 A and G23.43−0.18 B. Other transitions were also detected, but a discussion of the G23.43−0.18's chemistry is outside the scope of this work. In G23.43−0.18 A, the CH_3OH lines trace the shocked gas along the walls of the conical wide-angle bipolar outflow. Fig. 11 shows the moment 0 map of the 213.427 GHz CH_3OH line revealing parabolic structures consistent with the X-shape cavity traced by the redshifted and blueshifted emission of ^{12}CO. The 213.427 GHz CH_3OH emission lines up along the edges of the outflow cone walls. Similar structure has been reported in the Infrared Astronomical Satellite IRAS 16547−4247 protocluster in ^{12} CO($J = 3 - 2$) and CH_3OH ($J = 7 - 6$) (Higuchi et al. 2015).

In G23.43−0.18 B, all the CH_3OH transitions trace a rotating structure/disc at the centre of the core (see Fig. 12). Not all the CH_3OH transitions in G23.43−0.18 A show clear rotating structure (see Fig. 13). Some of the CH_3OH transitions (Fig. 13 left panel) appear to be tracing shocks from the walls of the wide-angle bipolar outflow, while others reveal compact emission with clear evidence of rotation (Fig. 13 right panel). The velocity gradient in G23.43−0.18 A is much shallower than in G23.43−0.18 B. This velocity gradient traces the rotation of the clump/envelope along a direction approximately perpendicular to that of the jet/outflow. The highest excitation temperature 230.368 CH_3OH line traces the inner part of the G23.43−0.18 B disc. The presence of a rotating disc and the observed collimated jet in G23.43−0.18 B points to the presence of a driving source in the centre of the object.

We tested for Keplerian rotation in G23.43−0.18 B by comparing position–velocity (PV) diagrams from our observations with synthetic Keplerian rotation models. The PV diagram was constructed for the three CH_3OH transitions (216.946, 217.299, and 229.589 GHz) along a line from ($18^h34^m39^s.208$, $-08°31'24''.998$) to ($18^h34^m39^s.176$, $-08°31'25''.678$). All three PV diagrams show an elongated, double-peaked structure. We generated synthetic models with the *thindisk* code (Maret 2019). The program generates a position–position–velocity (PPV) cube from which a PV diagram can be calculated. We used the model parameters shown in Table 3. We generated multiple models for different values of the stellar mass M_* and the inclination angle i. The least-squares difference between these models and our observations was then calculated. Fig. 14 shows the PV diagram for the three CH_3OH transitions and a well-fitting model where $M_* = 5\ M_\odot$ and $i = 60°$. Fig. 15 shows the least-squares error for all the values of M_* and i. These models reproduce the data well for $M_* \sin^2 i = 4\ M_\odot$. The 216 and 217 GHz lines also seem to imply inclination angles between 50° and 65°. We found a stellar mass of around 6 $M_\odot$. The presence of 6.7 GHz methanol masers in G23.43−0.18 B agrees with our findings that this YSO is sufficiently massive to excite this maser emission.

5 CONCLUSIONS AND SUMMARY

We reported the results of our ALMA 1.3 mm continuum and molecular line observations of G23.43−0.18. We detected five continuum cores G23.43−0.18 A, G23.43−0.18 B, G23.43−0.18 C1, G23.43−0.18 C2, and G23.43−0.18 C3. Blobs of dust continuum emission were seen around G23.43−0.18 A and spiral arm structure observed around G23.43−0.18 B. G23.43−0.18 A showed 'butterfly' morphology which is attributed to the existence of a cavity possibly ploughed by a wide-angle bipolar outflow. We resolved the wide angle outflow, as well as a bow structure ∼ 13000 au from the driving source. With molecular line tracers such as ^{12}CO and SiO, we traced the walls of an outflow cavity and calculated the outflow inclination angle to be 50°. We also calculated the momentum flux to be $4.06 \times 10^{-4}\ M_\odot$ km s^{-1} yr^{-1}, as well as other outflow parameters. We found the outflow parameters to be consistent with observations and simulations of HMYSOs. G23.43−0.18 B is

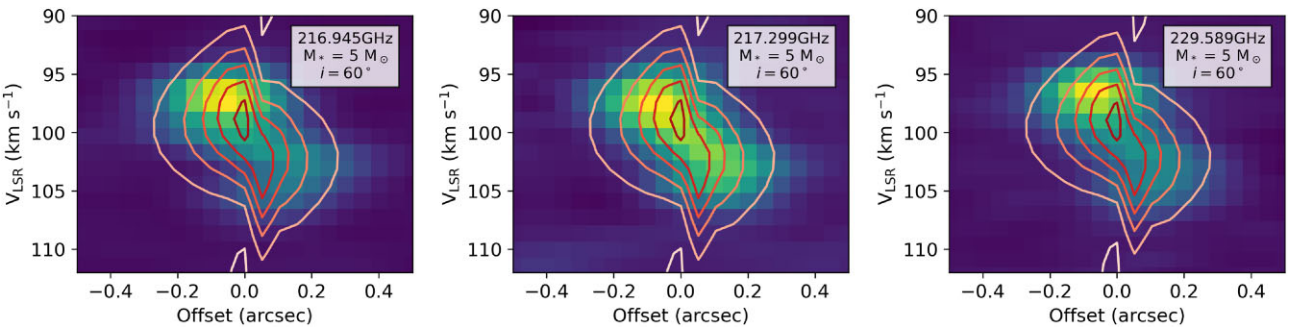

Figure 14. Comparison of CH_3OH position–velocity diagrams in G23.43−0.18 B to Keplerian models. The colour scale is the PV diagram from three CH_3OH lines while the contours show the Keplerian model for $M_* = 5\ M_\odot$ and $i = 60°$.

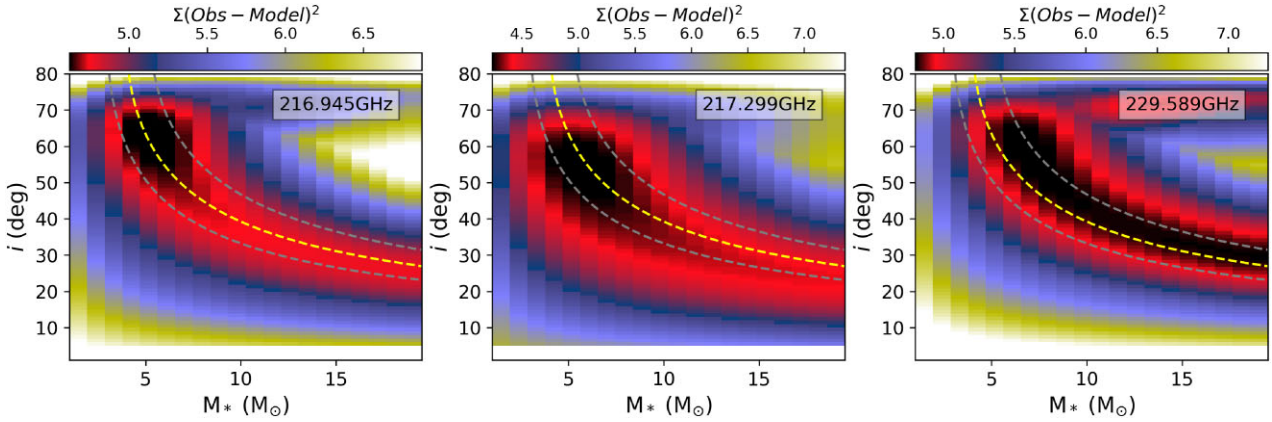

Figure 15. Sum of least-squares between the CH_3OH position–velocity diagrams and synthetic Keplerian models generated from *thindisk* (Maret 2019). The dashed lines show values of constant $M_* \sin^2 i$. The grey lines show where $M_* \sin^2 i$ is 3 and 5.3, respectively, while the yellow line shows where $M_* \sin^2 i = 4.0$.

associated with a jet, a rotating disc whose inner part exhibit Keplerian rotation. We traced compact CO emission along the jet axis, which may point to episodic ejections every $\sim$ 300 yr in the driving source.

ACKNOWLEDGEMENTS

JOC acknowledges support from the Italian Ministry of Foreign Affairs and International Cooperation (MAECI Grant Number ZA18GR02) and the South African Department of Science and Technology's National Research Foundation (DST-NRF Grant Number 113121) as part of the ISARP RADIOSKY2020 Joint Research Scheme. CJU is financially supported by the University of South Africa (Research Fund: 409000). AMS was supported by the Russian Ministry of Science and Higher Education, No. FEUZ-2023-0019. C.W.L. acknowledges support from the Basic Science Research Program through the NRF funded by the Ministry of Education, Science and Technology (NRF-2019R1A2C1010851) and from the Korea Astronomy and Space Science Institute grant funded by the Korea government (MSIT; project No. 2024-1-841-00). JMV acknowledges the National Research Foundation of South Africa grant number 134192 as well as the Research Council of Finland grant number 348342 for funding this research. TH is financially supported by the MEXT/JSPS KAKENHI Grant Numbers 17K05398, 18H05222, and 20H05845. Data analyses were in part carried out on common use data analysis computer system at the Astronomy Data Center, ADC, of the National Astronomical Observatory of Japan. This paper makes use of the following ALMA data: ADS/JAO.ALMA#2015.1.01571.S. ALMA is a partnership of ESO (representing its member states), NSF (USA) and NINS (Japan), together with NRC (Canada), MOST and ASIAA (Taiwan), and KASI (Republic of Korea), in cooperation with the Republic of Chile. The Joint ALMA Observatory is operated by ESO, AUI/NRAO, and NAOJ.

DATA AVAILABILITY

The raw data used in this paper can be obtained from the ALMA Science archive (ALMA#2015.1.01571.S). The fits images of the ALMA observations will be made available on reasonable request from the corresponding author.

REFERENCES

André Oliva G., Kuiper R., 2020, A&A, 644, A41
Beuther H. et al., 2017, A&A, 603, A10
Beuther H. et al., 2019a, A&A, 621, A122
Beuther H., et al., 2019b, A&A, 628, A90
Breen S. L., Ellingsen S. P., 2011, MNRAS, 416, 178
Breen S. L. et al., 2015, MNRAS, 450, 4109
Brogan C. L. et al., 2009, ApJ, 707, 1
Brogan C. L. et al., 2019, ApJ, 881, L39
Brunthaler A., Reid M. J., Menten K. M., Zheng X. W., Moscadelli L., Xu Y., 2009, ApJ, 693, 424
Burns R. A., et al., 2020, Nat. Astron., 4, 506
Caratti o Garatti A. et al., 2017, Nat. Phys., 13, 276
Caswell J. L., 2009, PASA, 26, 454
Caswell J. L., Vaile R. A., Ellingsen S. P., Whiteoak J. B., Norris R. P., 1995, MNRAS, 272, 96
Cesaroni R. et al., 1988, A&AS, 76, 445
Chen X. et al., 2020, Nat. Astron., 4, 1170
Chibueze J. O. et al., 2012, ApJ, 748, 146
Contreras Y. et al., 2013, A&A, 549, A45
Cunningham A. J., Klein R. I., Krumholz M. R., McKee C. F., 2011, ApJ, 740, 107
de Villiers H. M. et al., 2014, MNRAS, 444, 566
Dempsey J. T., Thomas H. S., Currie M. J., 2013, ApJS, 209, 8
Forster J. R., Caswell J. L., 1989, A&A, 213, 339
Forster J. R., Caswell J. L., 1999, A&AS, 137, 43
Frank A. et al., 2014, in Beuther H., Klessen R. S., Dullemond C. P., Henning T., eds, Protostars and Planets VI. Univ. Arizona Press, Tucson, p. 451
Frerking M. A., Langer W. D., Wilson R. W., 1982, ApJ, 262, 590
Fujisawa K. et al., 2014, PASJ, 66, 31
Goedhart S., Gaylard M. J., van der Walt D. J., 2004, MNRAS, 355, 553
Goldsmith P. F., Langer W. D., 1999, ApJ, 517, 209
Higuchi A. E., Saigo K., Chibueze J. O., Sanhueza P., Takakuwa S., Garay G., 2015, ApJ, 798, L33
Hirota T. et al., 2017, Nat. Astron., 1, 0146
Hogge T. et al., 2018, ApJS, 237, 27
Hu B. et al., 2016, ApJ, 833, 18
Hunter T. R. et al., 2017, ApJ, 837, L29
Ilee J. D. et al., 2016, MNRAS, 462, 4386
Ilee J. D. et al., 2018, ApJ, 869, L24
Johnston K. G. et al., 2015, ApJ, 813, L19
Johnston K. G. et al., 2020, A&A, 634, L11
Kang J.-. hyun., Byun D.-Y., Kim K.-T. Kim J., Lyo A. -Ran., Vlemmings W. H. T., 2016, ApJS, 227, 17
Kim J. et al., 2020, ApJ, 896, 127

Kim K.-T., Koo B.-C., 2003, ApJ, 596, 362
Kim K.-T. et al., 2018, Proc. IAU Symp. 336, Astrophysical Masers: Unlocking the Mysteries of the Universe, Cambridge University Press. p. 259
Kong S., Wu Y., 2011, MNRAS, 413, 71
Kuiper R., Hosokawa T., 2018, A&A, 616, A101
Kuiper R., Yorke H. W., Turner N. J., 2015, ApJ, 800, 86
Kuiper R., Turner N. J., Yorke H. W., 2016, ApJ, 832, 40
Liu H. B. et al., 2015, ApJ, 804, 37
Liu H. B. et al., 2019, ApJ, 871, 185
Liu S.-Y., Su Y.-N., Zinchenko I., Wang K-S., Wang Y., 2018, ApJ, 863, L12
Maret S., 2019, Zenodo, Thindisk,
Matsushita Y., Machida M. N., Sakurai Y., Hosokawa T., 2017, MNRAS, 470, 1026
Maud L. T., Moore T. J. T., Lumsden S. L., Mottram J.C., Urquhart J. S., Hoare M. G., 2015, MNRAS, 453, 645
Maud L. T. et al., 2019, A&A, 627, L6
McMullin J. P., Waters B., Schiebel D., Young W., Golap K., 2007, in Shaw R. A., Hill F., Bell D. J., eds, ASP Conf. Ser. Vol. 376, Astronomical Data Analysis Software and Systems XVI. Astron. Soc. Pac., San Francisco, p. 127
Menten K. M., 1991, ApJ, 380, L75
Meyer D. M.-A., Vorobyov E. I., Kuiper R., Kley W., 2017, MNRAS, 464, L90
Meyer D. M.-A., Kuiper R., Kley W., Johnston K. G., Vorobyov E., 2018, MNRAS, 473, 3615
Ossenkopf V., Henning T., 1994, A&A, 291, 943
Palagi F., Cesaroni R., Comoretto G., Felli M., Natale V., 1993, A&AS, 101, 153
Rogers H., Pittard J. M., 2013, MNRAS, 431, 1337
Rosen A. L., Krumholz M. R., 2020, AJ, 160, 78
Shirley Y. L. et al., 2013, ApJS, 209, 2
Slysh V. I., Kalenskii S. V., Val'TTS I. E., Golubev V., Mead K., 1999, ApJS, 123, 515
Sugiyama K., Saito Y., Yonekura Y., Momose M., 2019, Astron. Telegram, 12446, 1
Szymczak M., Kus A. J., Hrynek G., Kěpa A., Pazderski E., 2002, A&A, 392, 277
Szymczak M., Pillai T., Menten K. M., 2005, A&A, 434, 613
Szymczak M., Wolak P., Bartkiewicz A., Borkowski K. M., 2012, Astron. Nachr., 333, 634
Takahashi S. et al., 2008, ApJ, 688, 344
Tanabe Y. et al., 2019, PASJ, 71, S8
Tanaka K. E. I., Tan J. C., Zhang Y., 2016, ApJ, 818, 52
Tanaka K. E. I., Tan J. C., Zhang Y., 2017, ApJ, 835, 32
Torrelles J. M., Gomez J. F., Rodriguez L. F., Curiel S., Ho P. T.P., Garay G., 1996, ApJ, 457, L107
Valdettaro R. et al., 2001, A&A, 368, 845
Vlemmings W. H. T., Torres R. M., Dodson R., 2011, A&A, 529, A95
Walsh A. J., Burton M. G., Hyland A. R., Robinson G., 1998, MNRAS, 301, 640
Walsh A. J., Macdonald G. H., Alvey N. D. S., Burton M. G., Lee J. -K., 2003, A&A, 410, 597
Wood D. O. S., Churchwell E., 1989, ApJS, 69, 831
Xi H. et al., 2015, MNRAS, 453, 4203
Yang K. et al., 2019, ApJS, 241, 18
Yonekura Y. et al., 2016, PASJ, 68, 74

This paper has been typeset from a TEX/LATEX file prepared by the author.